ANL-80-33

ANL-80-33

ADVANCED FUEL CELL DEVELOPMENT

Progress Report for October—December 1979

by

R. D. Pierce, G. H. Kucera, D. S. Kupperman,
R. B. Poeppel, J. W. Sim, R. N. Singh,
and J. L. Smith

ARGONNE NATIONAL LABORATORY, ARGONNE, ILLINOIS

Prepared for the U. S. DEPARTMENT OF ENERGY
under Contract W-31-109-Eng-38

Distribution Category:
Energy Conversion
(UC-93)

ANL-80-33

Argonne National Laboratory
9700 South Cass Avenue
Argonne, Illinois 60439

ADVANCED FUEL CELL DEVELOPMENT

Progress Report for
October-December 1979

by

R. D. Pierce, G. H. Kucera, D. S. Kupperman,*
R. B. Poeppel,* J. W. Sim, R. N. Singh,* and
J. L. Smith

Chemical Engineering Division

May 1980

Previous reports in this series

July-September 1979	ANL-79-110
April-June 1979	ANL-79-84
January-March 1979	ANL-79-59
October-December 1978	ANL-79-28

*Materials Science Division, ANL.

TABLE OF CONTENTS

LIST OF FIGURES

LIST OF TABLES

CHEMICAL ENGINEERING DIVISION

ADVANCED FUEL CELL DEVELOPMENT

Progress Report for
October-December 1979

by

R. D. Pierce, G. H. Kucera, D. S. Kupperman,
R. B. Poeppel, J. W. Sim, R. N. Singh, and
J. L. Smith

ABSTRACT

This report describes advanced fuel cell research and development activities at Argonne National Laboratory (ANL) during the period October-December 1979. These efforts have been directed toward understanding and improving components of molten carbonate fuel cells and have included operation of 10-cm square cells.

The principal focus has been on the development of electrolyte structures ($LiAlO_2$ and Li_2CO_3-K_2CO_3) that have good electrolyte retention and mechanical properties as well as long-term stability. This effort included work on preparation of sintered $LiAlO_2$ as electrolyte support, use of a scanning laser acoustic microscope to evaluate electrolyte structures, and measurements of the thermal expansion coefficients of various mixtures of β-$LiAlO_2$ and carbonate eutectic.

SUMMARY

Development of Electrolyte Tiles

In the past, prior to the hot-pressing of $LiAlO_2/Li_2CO_3$-K_2CO_3 powder to form electrolyte tiles, graphite was sprayed on the pressing dies to act as a releasing agent. This has resulted in a thin graphite layer on the tiles, which may have a detrimental effect on cell performance. Therefore, means of removing this layer from fabricated tiles have been sought. The graphite was not removed when a fabricated tile was maintained in oxygen at 775 K for several hours. It has been removed from recent tiles with No. 600 abrasive paper.

In this report period, one electrolyte tile (T-1-5) was fabricated with a reinforcing screen, and two were fabricated without screens (T-1-24 and T-1-27). All three were free of cracks, but two had density variations that were detectable by X-radiography. An improved technique was developed to distribute the $LiAlO_2/Li_2CO_3$-K_2CO_3 powder in the die more uniformly; this technique involves the use of a small vibrating sifter. Each tile was heated to the hot-pressing temperature before the pressing load was applied; this has proved important to allow gas escape.

Development of Sintered $LiAlO_2$ Electrolyte Structures

Sintered $LiAlO_2$ structures of controlled pore size and porosity are being developed as an alternative to the paste structure as an electrolyte support. Because the α and β allotropes are more easily synthesized, they are being investigated as starting material prior to sintering; the sintered structures are always γ-$LiAlO_2$.

In this period, batches of both α- and β-$LiAlO_2$ powders were prepared for sintering. These powders contained little unreacted carbonates or hydroxides, which cause excessive densification during sintering, and little unreacted Al_2O_3, which causes excessive reaction and gas liberation when the sinter is impregnated with electrolyte. Sintering of these powders resulted in structures of $LiAlO_2$ with high porosity (about 60%). Sinters prepared from α-$LiAlO_2$ increased from 33 to 63% porosity when the cold-pressing pressure was decreased from 56 to 2 MPa; thus pressing pressure has a strong effect on the sintered porosity of α-$LiAlO_2$ samples. Sinters with porosities of about 58 to 60% were successfully impregnated with carbonates; higher porosities have lead to structural failures during impregnation.

The pore-size distribution for electrolyte structures is important to assure retention of electrolyte and avoid empty pores. The pore size should be smaller than that of the electrodes, and the size distribution should be narrow. Sintered samples prepared from α-, β-, and γ-$LiAlO_2$ were analyzed by mercury porosimetry. The samples prepared from α-$LiAlO_2$ had the smallest pores (50% of the volume in pores smaller than 0.12 μm) and the narrowest size distribution, and those prepared from γ-$LiAlO_2$ had the largest pores and widest size distribution. All of the sintered structures had mean pore sizes significantly smaller than those of the electrodes currently in use.

Nondestructive Evaluation of Electrolyte Structures

Electrolyte tiles were successfully examined using the scanning laser acoustic microscope (SLAM) of Sonoscan, Inc. at 30 MHz. Considerable variation in acoustic attenuation was found in the tiles. The observations suggest that local attenuation determination may provide a useful characterization parameter. Increased attenuation may be attributed to density changes or microfracturing. Introductory material on the SLAM is presented in this report along with the results on the tiles.

Testing of Electrolyte Structures

Studies have been initiated to determine the transformation temperatures of the $LiAlO_2$ allotropes. Heating of β-$LiAlO_2$ in a differential thermal analyzer and in a differential scanning calorimeter revealed a transformation at 959 ± 4 K to γ-$LiAlO_2$.

Compression tests were run on two pellets containing γ-$LiAlO_2$ and 69 vol % (62.5 wt %) carbonates. One pellet was heated to 775 K under a stress of 209 kPa, and the other under a stress of 41 kPa. Both slumped more than 50%; the former over a period of 30 s and the latter over several minutes. In a cell, a tile of this composition would lose electrolyte to the electrodes

and become less plastic. The results suggest that it would be desirable to begin the compressive loading of cells at the eutectic melting temperature (about 765 K) to have sufficient compliance to assure sealing and electrode-tile contact. Our cells have not been loaded until after they reach 925 K. Measurements are being made of the thermal expansion coefficient of various mixtures of β-$LiAlO_2$ and carbonate eutectic.

Cell Testing

Two 10-cm square cells were operated in this report period--SQ-14 and -15. Cell SQ-14 employed a screen-reinforced tile. The cell had electrical performance comparable to our best previous cell, SQ-9, and the lowest measured resistance to that date, 11 mΩ; however, a good wet seal was never attained. Cell SQ-15 used an unreinforced tile. The cell was loaded when the electrolyte was first melted, and better wet-seals were attained. The cell had the best electrical performance and lowest measured resistance, 8 mΩ, of our cells to date. Both cells SQ-14 and SQ-15 were run under load for about 200 h and each underwent corrosion of the 316 SS anode current collector. Nickel parts will be employed in the anode region as soon as the changes can be incorporated into future cells.

I. INTRODUCTION

The advanced fuel cell studies at Argonne National Laboratory (ANL) are part of the DOE Advanced Fuel Cell Program. A goal of this DOE program is the earliest possible introduction of high-efficiency generating systems based on molten-carbonate fuel cells, which have the capability of operating on coal or other fuels. At the present stage of development, the primary thrust of the ANL program is directed to development of the fuel cell itself.

A molten carbonate fuel cell consists of a porous nickel anode, a porous nickel oxide cathode, an electrolyte structure which separates the anode and cathode and conducts only ionic current between them, and appropriate metal housings or, in the case of stacks of cells, intercell separator sheets. The cell housings (or separator sheets) bear upon the electrolyte structure to form a seal between the environment and the anode and cathode gas compartments. The usual electrolyte structure, which is commonly called "tile", is a composite structure of discrete $LiAlO_2$ particles and a mixture of alkali metal carbonates. The carbonates are liquid at the cell operating temperature of 925 K. At the anode, hydrogen and carbon monoxide in the fuel gas react with carbonate ion from the electrolyte to form carbon dioxide and water while giving up electrons to the external circuit. At the cathode, carbon dioxide and oxygen react and accept electrons from the external circuit to re-form carbonate ion, which is conducted through the electrolyte to the anode. In a practical cell stack, CO_2 from the cathode probably would be obtained from the anode exhaust.

The ANL contribution to the program is intended to provide understanding of cell behavior and to develop improved components and processes. Improvements are needed in the electrolyte structure, which is receiving special attention at ANL. Characterization of tile properties and the relation of the properties to tile behavior in cells is of major importance. Determination of the stability of tile materials is also of high priority. Electrolyte structures employing a sintered $LiAlO_2$ matrix are being examined as an alternative to the paste-like tiles.

Cells are operated to assess the behavior of the electrolyte and other components and to understand the performance and life-limiting mechanisms at work within the cell. Cell operation is coupled with efforts on diagnostics and materials development.

II. DEVELOPMENT OF $LiAlO_2$ ELECTROLYTE TILES
(J. L. Smith and J. W. Sim)

In this report period, one tile with Kanthal screen reinforcement and two without were formed by the hot-pressing technique. All three were crack free, but two had some density variation which seems to be a function of the initial die loading.

The reinforced tile (T-1-5) was prepared from γ-$LiAlO_2$ and 62.5 wt % Li_2CO_3-K_2CO_3* (batch 134-113) as follows. The powder was dried in air at 725 K, and half of it was distributed in the die by hand with a spoon and leveled. A Kanthal screen was then placed in the die, and the balance of the powder applied with a small sifter. This deposited the powder in a doughnut shaped ring, which was then leveled throughout the die with an adjustable scraper that fitted in the die frame and remained parallel to its surface. The die was heated to the pressing temperature of about 750 K before pressure was applied. The tile was pressed for 0.5 h at 24 MPa (3500 psi). The load (including the top heater) was relieved from the die, and the die was cooled.

After the tile was removed from the die, an area of high graphite† density corresponding to the original doughnut-shaped powder pattern was observed on the surface of the tile. This area later was shown by X-ray radiograph‡ to have relatively high density. This seems to indicate a correlation between graphite transfer to the hot-pressed tile and tile density. It also seems to indicate that the material distribution in the die should be improved before pressing. No cracks were observed when the tile was wiped with an acetone-wetted paper; this has proved a sensitive means for detecting otherwise invisible cracks. X-ray examination also revealed no cracks.

Two tiles (T-1-24 and T-1-27) were pressed using γ-$LiAlO_2$ and 62.5 wt % Li_2CO_3-K_2CO_3 without a Kanthal reinforcing screen. The most significant procedural difference between the preparation of these and previous tiles is in the die loading. It is difficult to fill the die uniformly; and, in spite of leveling operations prior to pressing, the tile will exhibit density variations that correspond to the initial filling pattern. For these two most recent tiles, the die was filled using a vibrating sifter, which is a small cup that has a (1/4 × 7/8 in.) screen-covered slot in the bottom and is attached to a vibrator tool. Tile material was laid down in a 7/8-in. wide path in the die. Multiple orthogonal passes were made in order to fill the die as uniformly as possible. The leveling step with a scraper still followed, but much less powder movement was required to achieve a level surface than with earlier filling methods. These two tiles have been X-rayed. The first, T-1-24, had no cracks and appeared to be of a very uniform density. The second, T-1-27, had no cracks, but some density variation. This variation may have been caused by difficulty in leveling the material in the

---

*62 mol % Li_2CO_3-38 mol % K_2CO_3 unless otherwise indicated.

†Graphite is sprayed on the dies as a release agent prior to loading the $LiAlO_2$/Li_2CO_3-K_2CO_3.

‡X-ray radiography of tiles and sinters was performed by N. P. Lapinski Materials Science Division, ANL.

die due to a slight misalignment that was noted after assembly of the die components. The above described loading technique seems to result in a significant improvement in tile quality. Further improvement is desirable to improve both the speed and uniformity of the die loading.

In the past, the tiles that we fabricated had a thin surface layer of graphite on both faces after hot pressing. Attempts were made to eliminate graphite from tiles because it may be detrimental to cell performance. We were unable to remove graphite by maintaining a fabricated tile in oxygen at 725 K for several hours; we also were unsuccessful in avoiding graphite deposition on the tiles by buffing the die after spraying with graphite and before loading the powder. We have removed the graphite by sanding tile surfaces with No. 600 "wet-or-dry" paper.

III. DEVELOPMENT OF SINTERED $LiAlO_2$ ELECTROLYTE STRUCTURES

Sintered $LiAlO_2$ of controlled pore size and porosity is being investigated as an alternative electrolyte support to the paste structure used in the past. Although the sintered material is always γ-$LiAlO_2$, all three $LiAlO_2$ allotropes are being investigated as starting material prior to the sintering operation. The starting material for sinters is pure $LiAlO_2$; whereas, for tiles, the synthesis procedures were designed to produce a $LiAlO_2$-carbonate salt mixture.

A. Preparation and Sintering of α-$LiAlO_2$

(R. N. Singh, J. T. Dusek, D. J. Dorman, R. E. Mailhiot, and R. B. Poeppel)*

Past experiments (see, for example, ANL-79-110, p. 9) demonstrated that samples in the form of disks (about 3-cm dia) and plates (about 13 × 13 cm) with porosities as high as 64% can be fabricated from α-$LiAlO_2$ powder. It was also established that "pock marks" that occurred on sintering some plate samples were due to unreacted Li_2CO_3 in the powder. Therefore, attempts are now being made to prepare α-$LiAlO_2$ powders with as little unreacted Li_2CO_3 as possible by controlling the ratio of γ-Al_2O_3 to Li_2CO_3 reactants and by better mixing of the starting powder.

A summary of the preparation method is given in Table 1 for three batches of powders that were mixed and reacted at temperatures between 873 and 923 K for up to 72 h to produce α-$LiAlO_2$. Plates were fabricated from batches RJ-1 and -2 and sintered at about 1223 K for about 2 h. In both cases, the sintered structures were severely warped; this was attributed to the presence of small amounts of unreacted Li_2CO_3 in the starting powder. The next batch (RJ-4) was prepared with about 8 wt % more Degussa γ-Al_2O_3. A thermogravimetric analysis† of this Al_2O_3 indicated 7.1 wt % moisture when the sample was heated to a maximum temperature of 873 K. Most of the water was removed at a lower temperature (<573 K), thereby indicating a predominance of adsorbed moisture. A small disk sample prepared from batch RJ-4 was sintered at 1173 K for 2 h and resulted in a sintered structure with about 58% porosity. Scanning electron microscopic (SEM) examination of the microstructure revealed unreacted Li_2CO_3; therefore, this powder was further heat treated to complete the reaction. The resulting powder (RJ-4-1) was used to press another disk sample, which was sintered at 1173 K for 2 h; this treatment resulted in a sintered sample with 59% porosity. The X-ray analyses performed on the RJ-4 and RJ-4-1 powders did not detect unreacted Li_2CO_3.

Two additional batches (RJ-5 and -6) of powder were mixed and reacted at 923 K for 95.5 h (Table 2). After reacting, the powders were sieved through 60-mesh screen before pressing into pellets. Disks and a plate were pressed from these powders. The compacting pressure was varied to study its influence on porosity levels after pressing as well as sintering; the results

---

*Materials Science Division, ANL.

†Thermogravimetric analysis was run in the Analytical Chemistry Laboratory, ANL.

Table 1. Summary of Powder Preparation Method

Batch No.	Constituent Ratio, γ-Al_2O_3 (Degussa) & Li_2CO_3	Temp., K	Time, h	$LiAlO_2$ Allotrope[a]	Results of Sintering
RJ-1	Stoichiometric,[b] dry mixed	873	50	α	Warping, liquid phase present
RJ-2	Stoichiometric,[b] wet mixed in ethanol	873	50	(v.mi. Li_2CO_3)	Warping, liquid phase present
RJ-4	8 wt % excess Al_2O_3 reagent,[c] wet mixed in ethanol	873	72	α	Some liquid phase after sintering
RJ-4-1	Further heat treatment of RJ-4	873 923	15.5 24	α	Some liquid phase after sintering

[a]Determined by X-ray analysis of powder.

[b]Assuming both reagents are pure.

[c]The γ-Al_2O_3 was shown to contain about 7% water in an analysis performed before preparation of Batch RJ-4.

Table 2. Summary of Improved Powder Preparation Method

Batch No.	Preparation Method
RJ-5	Li_2CO_3 dissolved in 1550 cc of methanol, then stoichiometric Al_2O_3[a] added slowly while mixing. The slurry was wet ball milled for 21.5 h. The slip was centrifuged at 1700 rpm for 10 min., hood and vacuum dried, crushed and sieved through 60-mesh screen. Reacted at 923 K for 95.5 h.
RJ-6	Dry mixed for 22 h with five small rubber stoppers. The mixed powder was sieved through 60-mesh screen. Reacted at 923 K for 95.5 h.

[a]Degussa γ-Al_2O_3; 8% excess Al_2O_3 reagent added to compensate for water content.

are summarized in Fig. 1. For the disks, as the compacting pressure was decreased from 56 to 2 MPa, porosity after pressing increased from 56 to 76% and the porosity after sintering increased from 33 to 63%. Therefore, compacting pressure is important in controlling the porosity of sintered samples prepared from α-$LiAlO_2$ powders. The plate sample (28-P) shown in Fig. 1 had a higher porosity (66%) after sintering than the similarly pressed and sintered disks.

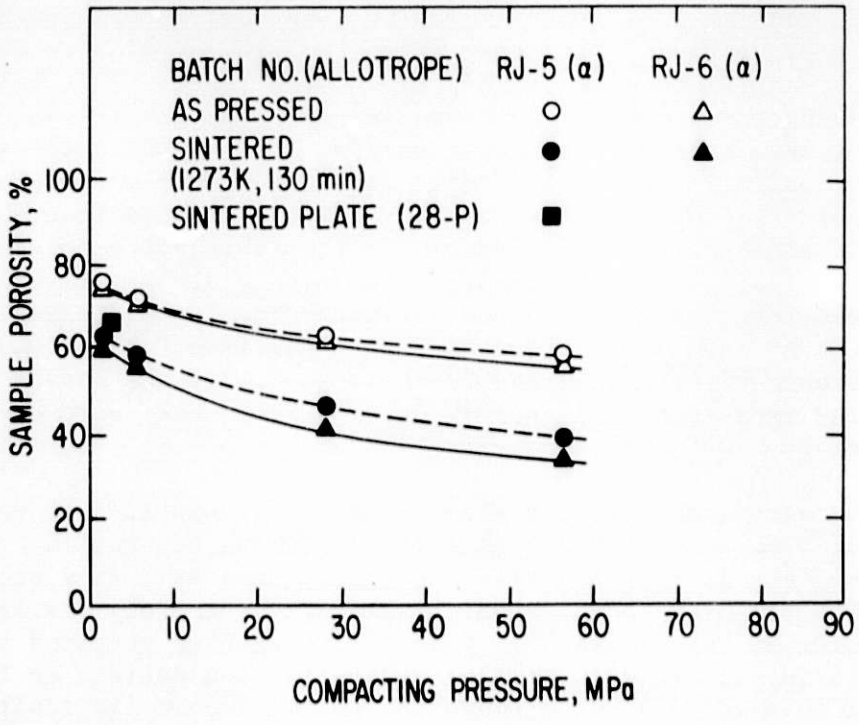

Fig. 1. Influence of Compacting Pressure on Sample Porosity

B. Preparation and Sintering of β-$LiAlO_2$

(J. W. Sim)

Previously (ANL-79-110, p. 4), we had difficulty in obtaining high-porosity sintered structures from γ-$LiAlO_2$ powders. During periods of high relative humidity such as the summer months, agglomeration of the Li_2CO_3 and Al_2O_3 reactants resulted in low-surface-area γ-$LiAlO_2$, and pellets pressed from such powders had low porosities. To avoid the problems associated with mixing of powdered reactants, we investigated the fabrication of sintered structures from β-$LiAlO_2$ prepared by impregnating alumina (or hydrated alumina) with an aqueous solution of LiOH, drying the resulting slurry, and reacting the dried powder. Sinters of greater than 60% porosity were routinely obtained from β-$LiAlO_2$ prepared by this method, provided that mixing of the aqueous slurry of alumina and lithium hydroxide was adequate (see ANL-79-110, p. 6). During the sintering step, the β-$LiAlO_2$ was transformed to γ-$LiAlO_2$.

Four types of alumina--ALCOA types C-33, H-705, and H-710 $Al(OH)_3$ and Degussa γ-Al_2O_3--were used as reactants to produce β-$LiAlO_2$. The characteristics of these aluminas were given in Table 3. The slurry preparations are summarized in Table 4; after drying the slurry in an oven at about 425 K, the dried powders were heat treated to complete the reaction to form β-$LiAlO_2$. The heat treatment conditions and the β-$LiAlO_2$ product characteristics are given in Table 5. Pellets (about 2.9-cm dia and about 0.2-cm thick) were pressed at 27.6 kPa and sintered according to the conditions in Table 6 to determine whether high-porosity sinters could be obtained from each of the β-$LiAlO_2$ powders.

Two methods of impregnating the alumina were employed. In the first method, the alumina powder was added to a stirred solution of LiOH in water. When high-surface-area aluminas (H-705 and Degussa) were impregnated by this technique, a gel formed during the addition of the alumina to the LiOH solution, preventing adequate mixing of the reactants. This gel formation occurred during the preparation of samples 134-105, 134-110 and 159-109b (see Table 4); pellets pressed from these samples (first five pellets in Table 6) densified excessively upon sintering. Sample 159-109b was washed* to remove the LiOH and/or Li_2CO_3 from the sample. Pellets pressed from this washed β-$LiAlO_2$ did not densify upon sintering. From this, we concluded that a liquid film of LiOH or Li_2CO_3, resulting from inadequate mixing of the alumina with the LiOH solution, was promoting densification during sintering. The two samples prepared from low-surface-area alumina [type C-33 $Al(OH)_3$], by the first technique, 134-117 and 134-120 in Table 4, did not form a gel during the mixing of the reactants; and pellets pressed from these samples did not densify upon sintering.

For the second method, the alumina was first slurried in water, and then the LiOH solution was added to the stirred alumina suspension. An advantage of this technique is that the reactant slurry becomes less viscous as the LiOH solution is added to the alumina suspension, thereby permitting better overall mixing of the reactants. None of the samples prepared by the second mixing technique densified upon sintering (last ten pellets in Table 6). In these samples, a gel did not form during the mixing of the reactants, and

*Washed with a mixture of equal volumes of acetic acid and acetic anhydride and then with methanol.

Table 3. Characteristics[a] of Alumina Used to Prepare β-$LiAlO_2$ for Sintered Structures

Type	Surface Area, m^2/g	Loose Bulk Density, g/cm^3	Particle Size Distribution	
			Size, μm	Percentage
C-33 $Al(OH)_3$	0.1-0.2	0.95-1.15	>149	0-1%
			>74	5-10%
			>44	30-60%
			<44	40-70%
H-710 $Al(OH)_3$	6-8	0.13-0.22	<2	100%
			<1	85%
			<0.5	28%
H-705 $Al(OH)_3$	12-15	0.08-0.14	<2	100%
			<1	99.5%
			<0.5	60%
Degussa Al_2O_3	100 ± 15	0.064	0.02 μm (avg.)	

[a]Manufacturer's specifications.

the presence of unreacted LiOH (or Li_2CO_3) was apparently minimized. Although Li_2CO_3 was detected by X-ray diffraction analysis in some of these samples (159-134 and 159-136), it probably was dispersed sufficiently to avoid promoting densification. Thus, we believe that high-porosity sinters can be obtained from β-$LiAlO_2$ powders if the alumina is well mixed with the LiOH solution. Our experience indicates that the second impregnation technique results in better reactant mixing when high-surface-area aluminas are used and consistently produces β-$LiAlO_2$ that does not densify upon sintering.

As discussed in the next section, extensive gas evolution was observed when the sintered plates fabricated from sample 159-139 were impregnated with molten carbonate eutectic. This gas apparently was produced by the reaction of Li_2CO_3 in the molten eutectic with small amounts of unreacted Al_2O_3 in the sintered plates. Subsequently, samples were pressed and sintered from powder containing 5 mol % additional LiOH. These samples did not densify during sintering; thus, a small amount of LiOH can be used to prepare β-$LiAlO_2$ without promoting densification. We plan to determine whether gas evolution is avoided during impregnation when sinters are prepared with this excess LiOH.

Table 4. Summary of Slurry Conditions Used to Prepare β-$LiAlO_2$

Sample No.	Type of Alumina	Moles[a] $LiAlO_2$	Li-to-Al Mole Ratio	Volume H_2O, L	Mixing Technique	Comments
134-105	ALCOA H-705	1.36	1.02	1.00	b	Gel formed
134-110	ALCOA H-705	1.36	1.01	0.50	b	Gel formed
159-109b	Degussa	1.34	1.02	0.75	b	Gel formed
134-117	ALCOA C-33	0.68	1.01	0.25	b	No gel formed
134-120	ALCOA C-33	2.08	1.00	0.75	b	No gel formed
159-134	Degussa	1.37	1.02	1.06	c	No gel formed
159-136	ALCOA H-705	1.38	1.01	1.26	c	No gel formed
159-137-1	Degussa	1.37	1.02	1.06	c	No gel formed
159-137-2	ALCOA H-705	1.38	1.01	1.26	c	No gel formed
159-139	Degussa	1.84	0.99	1.32	c	No gel formed
159-142a	ALCOA H-710	1.31	1.05	1.00	c	No gel formed
159-145a	ALCOA H-710	1.31	1.05	0.55	c	No gel formed
159-145b	ALCOA H-710	1.31	1.05	0.55	c	No gel formed

[a]Based on limiting reactant.

[b]Alumina was added to LiOH solution.

[c]Alumina slurry was formed, then LiOH solution was added to the alumina slurry.

Table 5. Heat Treatment and Characteristics of β-$LiAlO_2$

Sample No.	Heat Treatment Temperature, K	Time, h	X-ray Analyses[a]	Surface Area, m^2/g
134-105	725	3.5	β-$LiAlO_2$ (maj.) poss. γ-Al_2O_3 (mi.)	13
134-110	725	2	β-$LiAlO_2$ (maj.) poss. γ-Al_2O_3 (v. mi.)	18
159-109b	725	2	β-$LiAlO_2$ (maj.) Li_2CO_3 (mi.) γ-Al_2O_3 (v.mi.)	34
134-117	750	1.5	β-$LiAlO_2$ (maj.) γ-Al_2O_3 (mi.)	41
134-120	725	1.5	β-$LiAlO_2$ (maj.) γ-Al_2O_3 (mi.)	42
159-134	725	3.5	β-$LiAlO_2$ (maj.) Li_2CO_3 (med.) γ-Al_2O_3 (med.)	32
159-136	725	3.5	β-$LiAlO_2$ (maj.) Li_2CO_3 (med.) $LiH(AlO_2)_2 \cdot 5H_2O$ (mi.) γ-Al_2O_3 (v. mi.)	--
159-137-1	725 825	1 1	—	--
159-137-2	725 825	1 1	—	--
159-139	725 875	1.5 1.5	β-$LiAlO_2$ (maj.) γ-Al_2O_3 (v. mi.)	--
159-142a	725	1.5	β-$LiAlO_2$ (maj.) γ-Al_2O_3 (v.v. mi.)	38
159-145a	725	1.5	β-$LiAlO_2$ (only)	—
159-145b	725 925	1.5 1.5	β-$LiAlO_2$ (maj.) γ-$LiAlO_2$ (mi.) γ-Al_2O_3 (v. mi.) α-$LiAlO_2$ (poss. v. mi.)	—

[a]Abbreviations used in this table are as follows: maj. = major; med. = medium; mi. = minor; v. = very; and poss. = possibly.

Table 6. Results of Sintering β-$LiAlO_2$

Pellet No.	Sample No.	Sintering Temp., K	Sintering Time, h	Cold-Pressed[a] Porosity, %	Sintered Porosity, %
105-1	134-105	1400	1	61.1	32.5
110-1	134-110	1175	3	58.3	30.4
P-159-128-1	134-110	875 1265	23 0.1	56.5	20.1
P-159-128-2	159-109b	875 1265	23 0.1	53.1	31.2
P-126-2	159-109b	875 1265	3 0.75	53.8	31.8
P-126-3	159-124	875 1265	3 0.75	55.1	55.1
159-124	159-124	1265	1	54.3	53.9
P-126-1	134-120	875 1265	3 0.75	60.1	61.1
P-159-132-4	134-117	1265	0.5	60.0	61.7
P-159-135-1	159-134 (+100 mesh)	1265	0.5	63.9	62.5
P-159-135-2	159-134 (-100 mesh)	1265	0.5	62.7	63.9
P-159-136	159-136	875 1265	1 0.5	65.4	67.5
P-159-138-1	159-137-1	1265	0.75	60.4	61.4
P-159-138-2	159-137-2	1265	0.75	63.8	63.5
P-159-140-1	159-139 (-100 mesh)	1265	0.5	64.4	64.7
P-159-140-2	159-139 (-60 mesh, +100 mesh)	1265	0.5	63.3	63.8
P-159-142	159-142a	1265	0.5	64.0	63.5
P-159-145a	159-145a	1265	0.5	62.7	64.3
P-159-145b	159-145b	1265	0.5	62.2	62.2

[a]Pressed at 27.6 kPa.

C. Impregnating Sintered Plates

(R. N. Singh, J. T. Dusek, R. E. Mailhiot, D. J. Dorman, and R. B. Poeppel)*

Sintered plates prepared from α- and β-$LiAlO_2$ powders were impregnated with Li_2CO_3-K_2CO_3 in a vacuum. The results of this impregnation are summarized in Table 7. Sample 26-P, which contained significant unreacted Li_2CO_3, showed warpage and cracking due to weakening of the sintered bonds during impregnation with molten carbonates. Small sections popped out from the surface of samples 28-P, 25-P, and 27-P--apparently because of pressure produced by gas generated through the reaction of Li_2CO_3 in the melt with unreacted alumina in the sintered plate. The presence of popped-out sections only at the outer edges of sample 28-P may be a result of higher porosity and/or large voids in these locations. To avoid porosity variations in the sinter, a method (discussed in Section II) of loading the die more uniformly was tried. Sample 31-P was sintered to a lower porosity level (58%), to improve the strength of the plate, and impregnated with molten carbonates under ambient pressure instead of a vacuum to reduce pressure differentials produced by the evolved gas. This procedure resulted in an impregnated sample with no pop-outs or visible cracks. Therefore, crack-free impregnated samples can be fabricated from α-$LiAlO_2$ powders prepared by ball milling the Al_2O_3 and Li_2CO_3 reactants in methanol (batch RJ-5 in Table 2). This α powder, which is Li_2CO_3 free, also can be used to prepare γ-$LiAlO_2$ powder through heat treatment of the powder at temperatures of 1050 to 1100 K. Plates of about 60% porosity fabricated from β-powders containing a slight excess of LiOH will be impregnated in the future. Plates fabricated from the $LiAlO_2$ powders should be restrained by a cover plate during firing to avoid warpage.

D. Characterization of Sintered $LiAlO_2$

(J. W. Sim, R. N. Singh)

The pore-size distribution in the components of molten carbonate fuel cells greatly affects cell performance. This parameter must be adjusted for each component (anode, cathode, electrolyte) so that during cell operation the electrodes become wetted, but not flooded, by the molten carbonates. Removal of large amounts of carbonates from the electrolyte structure by the electrodes must also be avoided; this would create open porosity in the electrolyte structure and might permit cross-leakage of reactant gases. Characterization of the pore structure of the $LiAlO_2$ matrix in paste-type electrolyte structures is difficult because (1) the $LiAlO_2$ particles are not bonded to one another and (2) removal of the carbonates from such a structure would destroy the orientation of the $LiAlO_2$ particles with respect to one another. In sintered $LiAlO_2$ structures, however, the particles are bonded to one another. As a result, the pore structure is well-defined and easily characterized by mercury porosimetry. Therefore, we analyzed several specimens of sintered $LiAlO_2$ by mercury porosimetry to determine their porosities and pore size distributions.

The results of these analyses for samples prepared from all three allotropic forms of $LiAlO_2$ are given in Table 8. The conditions used to prepare sinters from β-$LiAlO_2$ powders were presented in Table 6, while the conditions

*Materials Science Division, ANL.

Table 7. Results of Impregnation of Sintered Structures

Sample No.	Starting Powder Batch	Allotrope	Cold Press Load, MPa	Sintering Temp., K	Sintering Time, h	Sintered Porosity, %	Method of Impregnation (925 K)	Results of Impregnation
26-P	RJ-4[a]	α	6.6	1225	2	54	Vacuum, step-wise immersion	Sample warped, cracked, & pop-outs.
28-P	RJ-5[b]	α	2.8	1275	2	66	Vacuum, continuous immersion	Pop-outs on outer edges; gas evolution during immersion.
25-P	159-139[c]	β	13.8	1375	2	69	Vacuum, step-wise immersion	Sample cracked, pop-outs; gas evolution during immersion.
27-P	159-139[c]	β	13.8	1373	2	65	Vacuum, continuous immersion	Pop-outs only at the top edge which was thicker; gas evolution during impregnation.
31-P	RJ-5[b]	α	2.8	1375	1/2	58	Air, continuous immersion	No cracks or pop-outs.

[a]Prepared as described in Table 1.

[b]Prepared as described in Table 2.

[c]Prepared as described in Tables 4 and 5.

Table 8. Physical Properties of Sintered $LiAlO_2$ Structures and of Typical Electrodes

Sample No.	10% Pore Volume Smaller Than This Diameter, μm	50% Pore Volume Smaller Than This Diameter, μm	90% Pore Volume Smaller Than This Diameter, μm	Porosity %
53[a]	0.06	0.11	0.16	60.6
37[a]	0.09	0.12	0.16	58.4
41[a]	0.09	0.12	0.16	58.5
45[a]	0.09	0.12	0.16	48.3
49[a]	0.09	0.13	0.17	47.9
57[a]	0.09	0.12	0.16	23.6
55[b]	0.11	0.22	0.87	56.4
39[b]	0.17	0.30	1.24	53.5
43[b]	0.17	0.30	1.28	54.8
47[b]	0.17	0.28	1.16	51.3
51[b]	0.21	0.72	2.39	57.5
59[b]	0.20	0.53	1.80	48.0
P-126-3[c]	0.05	0.16	0.33	57.2
P-159-140-2[c]	0.11	0.24	0.40	62.9
P-159-138-1[c]	0.13	0.26	0.41	60.3
P-159-138-2[c]	0.17	0.27	0.40	61.8
P-159-140-1[c]	0.14	0.29	0.42	64.7
P-159-135-1[c]	0.10	0.30	0.49	65.1
P-159-135-2[c]	0.11	0.30	0.57	63.7
P-159-136[c]	0.19	0.32	0.78	69.1
P-159-142[c]	0.20	0.32	0.42	62.1
P-126-1[c]	0.04	0.37	0.97	60.4
P-159-132-4[c]	0.07	0.50	1.30	60.5
Typical Anode	2.9	4.6	7.8	63.8
Typical Cathode[d]	3.8	9.6	20.2	74.4

[a]Prepared from α-$LiAlO_2$.

[b]Prepared from γ-$LiAlO_2$.

[c]Prepared from β-$LiAlO_2$.

[d]Before in situ oxidation.

used to prepare sinters from α- and γ-$LiAlO_2$ powders were reported previously (ANL-79-84, p. 10). The data in the third column of Table 8 are commonly referred to as the mean pore size of the specimen, while the data in the second and fourth columns indicate whether the pore size distribution of the specimen is broad or narrow. In general, the pellets prepared from β-$LiAlO_2$ have mean pore sizes comparable to pellets prepared from γ-$LiAlO_2$ but larger than those of pellets prepared from α-$LiAlO_2$. Also, the pellets prepared from β-$LiAlO_2$ have narrower pore size distributions than the pellets prepared from γ-$LiAlO_2$; the pellets prepared from α-$LiAlO_2$ have the narrowest pore size distributions, however. Of the pellets prepared from β-$LiAlO_2$, P-126-1 and P-159-132-4 had the broadest pore size distributions and the highest mean pore sizes. This was not unexpected because the powders used in these pellets were prepared from the relatively coarse (see Table 3) ALCOA Type C-33 alumina. Coarse particles should produce larger pores and, when mixed with some fine particles, should produce a broad pore-size distribution. The porosities of the pellets prepared from β-$LiAlO_2$ were generally higher than those of the pellets prepared from either α- or γ-$LiAlO_2$.

Ideally, $LiAlO_2$ sinters used in electrolyte structures should possess high porosities and small pore sizes. In sinters of high porosities, the amount of non-conducting $LiAlO_2$ in the electrolyte structure is minimized, thereby producing low electrical resistance. The small pores retain the molten carbonates within the electrolyte structure by capillary action during cell operation. All of the $LiAlO_2$ sinters in Table 8 have pore sizes that are much smaller than the pore sizes of typical electrode materials. Indeed, the mean pore sizes of most of the $LiAlO_2$ sinters are an order of magnitude smaller than the mean pore sizes of typical electrodes. However, only the pellets prepared from β-$LiAlO_2$ have porosities consistently greater than 60%.

IV. EVALUATION OF ELECTROLYTE TILES

(D. S. Kupperman,* D. E. Yuhas,† C. Vorres,† R. B. Poeppel*)

Electrolyte tiles were investigated using a scanning laser acoustic microscope (SLAM) operating at 30 and 100 MHz. The goal of the initial investigations was to determine testing feasibility. (Introductory material on the SLAM and the type of data that are obtained with it is presented in an appendix.) Two tiles (T-159-112 and T-1-5) were sent to Sonoscan, Inc. for testing. Sample T-159-112 previously had been broken in three places. Initially, the tiles were examined using both shear- and compressional-wave insonification at 100 MHz. In both cases, the samples were found to attenuate sound too much at this frequency for ultrasonic characterization. Subsequently, the samples were examined at 30 MHz. At this frequency, high-quality acoustic micrographs were obtained. The results of these initial investigations are presented below.

Photographs were taken in five areas of sample T-159-112, labeled "A" to "E" in Fig. 2. The area with the best acoustic transmission occurred at "C" (Fig. 3a). At location "A", considerably less transmission occurred (10 dB less than "C"), but fringes were still apparent (Fig. 3b). Area "B" (Fig. 3c) shows an interface between regions with no transmission and one with very little. Another interface at "D" (Fig. 3d) is shown between areas of good and lesser transmission. A small patch of attenuation was found at "E" (Fig. 3e). Overall, Tile T-159-112 had a very marbled appearance.

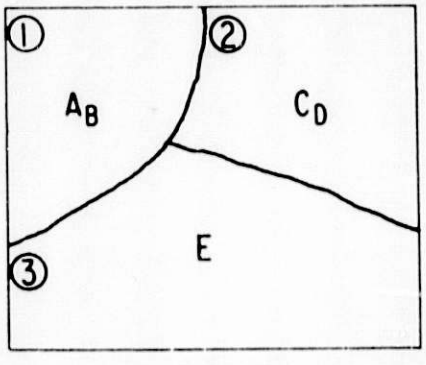

Fig. 2. Schematic of Regions of Tile T-159-112 Examined by Acoustic Microscopy

The transmission through Tile T-1-5 was very good, resembling area "C" of T-159-112. The overall texture was similar to that of the other tile, but fewer gradients of attenuation were found. Figure 4 shows a dark, diagonal line observed in one corner, which upon closer examination was found to be a crack. A small dark blotch was also found as shown in the diagram.

---

*Materials Science Division, ANL.

†Sonoscan, Inc., Bensenville, IL 60106.

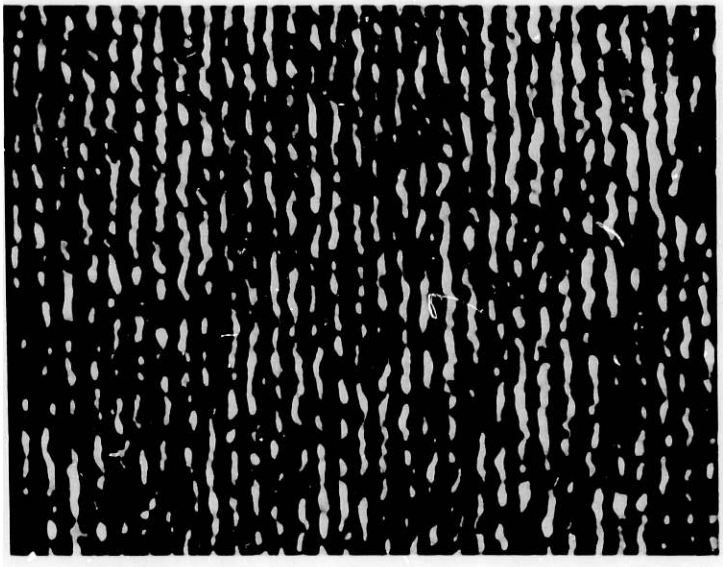

(a) Region C.

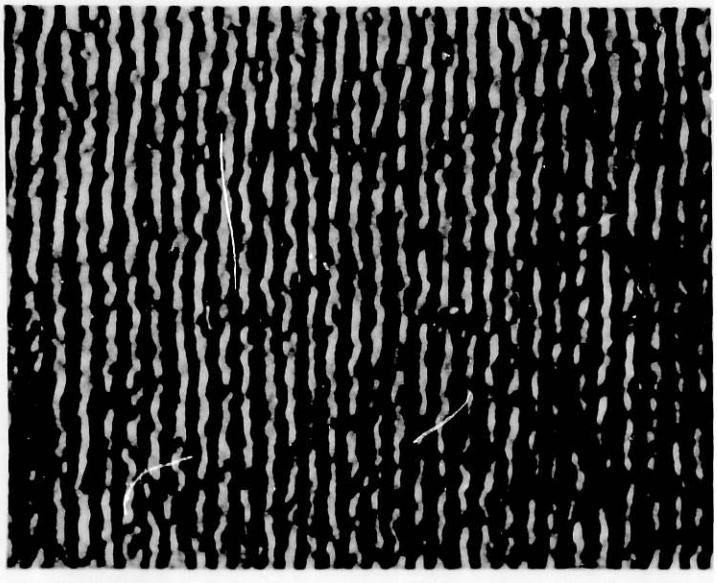

(b) Region A.

Fig. 3(a-e). Interferograms Taken from Tile T-159-112. (In each, the horizontal field of view is 1 cm.)

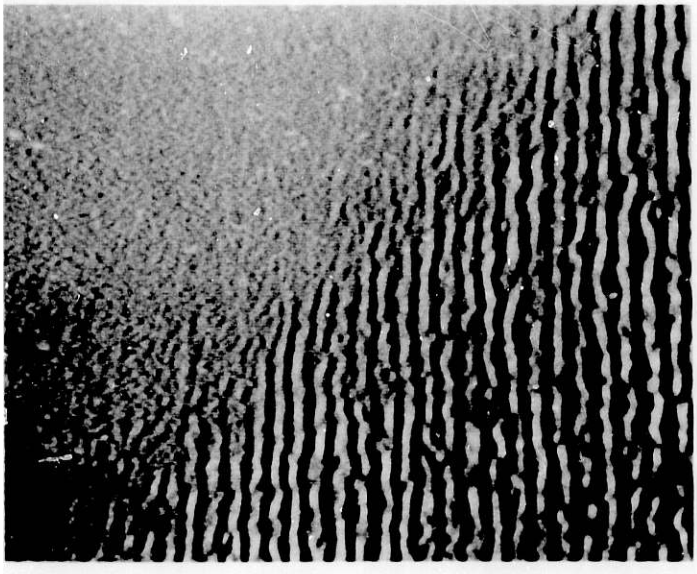

(c) Region B.

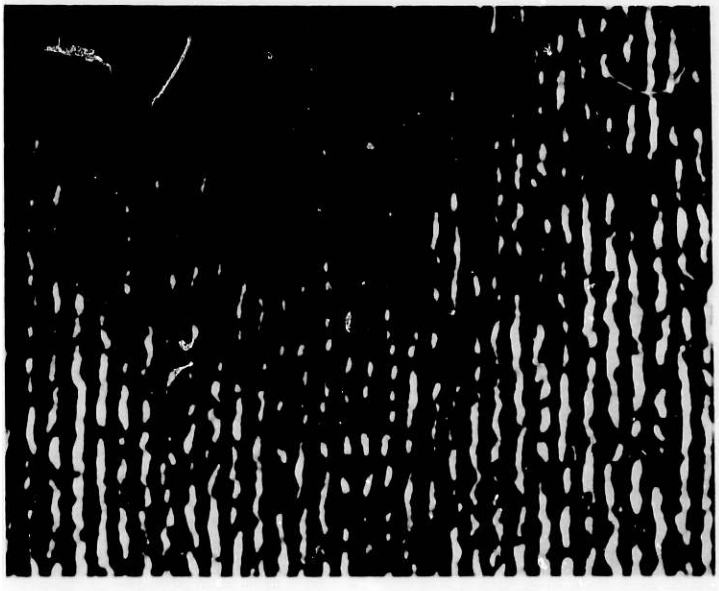

(d) Region D.

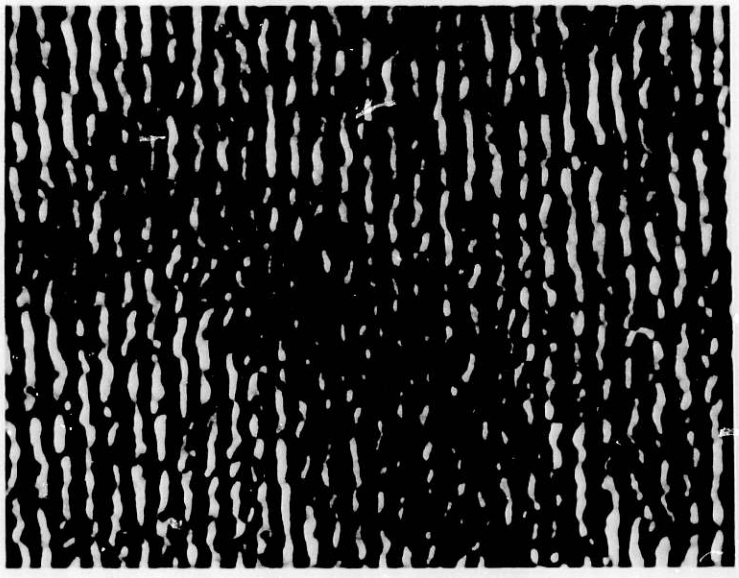

(e) Region E.

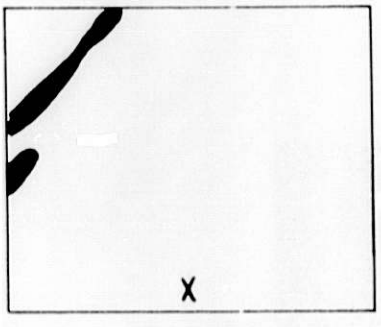

Fig. 4.

Schematic of Crack Indication in Tile T-1-5 ("X" mark for orientation purposes)

Because tiles are soluble in water, their exposure to water was kept to a minimum. However, approximately 15 to 30 min. were required to scan, photodocument, and mark sample T-159-112; during this time, the sample was totally submerged in water. After this initial examination, the tiles were towel dried and appeared to have suffered no adverse effects. Twelve hours later, when the tiles were reexamined, no sound would propagate through either of the samples. Obviously, the water exposure had a deleterious effect that precludes using water for nondestructive evaluation of these tiles. Two approaches can be used to overcome this problem: (a) the sample can be totally submerged in a fluid compatible with both the tiles and the SLAM, e.g., a hydrocarbon, or (b) the sample could be enclosed in plastic bags filled with a fluid compatible with the tile. The tiles could be tested through the bag as shown schematically in Fig. 5.

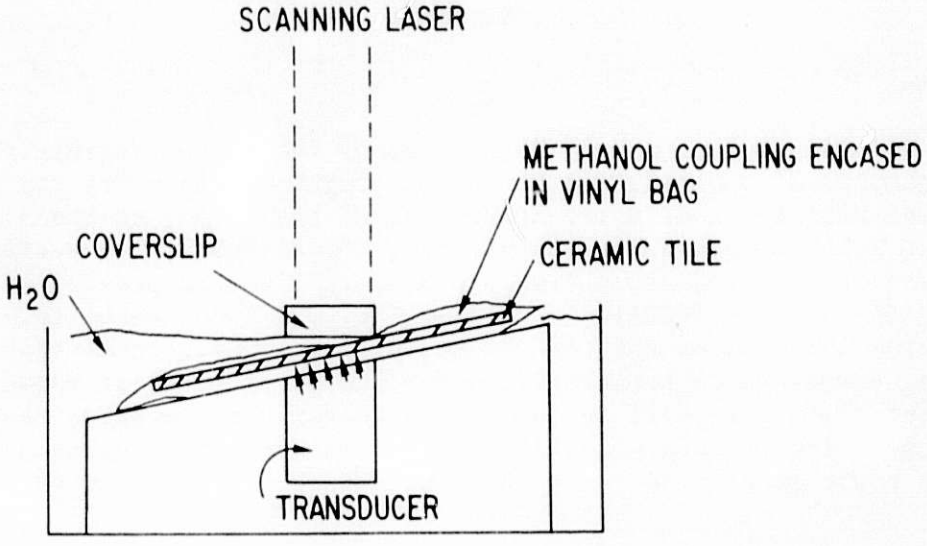

Fig. 5. Acoustic Coupling Scheme for Nonaqueous Imaging

This study has indicated the following:

(a) Intact tiles are compatible with the SLAM operating at 30 MHz.

(b) Considerable variation in acoustic attenuation was found in the two tiles examined (25 dB). These observations suggest that local attenuation determinations may provide the best measurement of tile quality. Increased attenuation can be attributed to density changes or microfracturing.

(c) Water contact with samples is not suitable for nondestructive testing.

V. TESTING OF ELECTROLYTE STRUCTURES
(G. H. Kucera)

A. Thermal Stability Testing

In previous studies (ANL-77-29, p. 15) on the thermal stability of powdered samples of β-$LiAlO_2$ and 55 wt % Li_2CO_3-K_2CO_3 in a dry CO_2 environment, it was reported that a transformation of the $LiAlO_2$ to the γ allotrope occurred at 925 K within about 100 h. However, at 925 K, the average fuel cell temperature, no transformation was observed in cold-pressed pellets containing mixtures of β-$LiAlO_2$ and 55 wt % Li_2CO_3-K_2CO_3 eutectic, even after 5000 h in the CO_2 environment (ANL-79-84, p. 20). The thermal stability of β-$LiAlO_2$ at temperatures between 925 and 975 K is of interest because sections of the electrolyte tile will be exposed to temperatures greater than the average cell operating temperature (925 K). For example, the region near the gas outlets in power generating cells in a fuel stack are expected to be at about 975 K.

In the current studies, cold-pressed pellets (about 85% theoretical density) containing β-$LiAlO_2$ and 55 wt % Li_2CO_3-K_2CO_3 were heated in a dry CO_2 environment to 950 K. The β-$LiAlO_2$ was prepared by a water-slurry technique in which a stoichiometric amount of Degussa γ-Al_2O_3 was added to a stirred and heated (about 365 K) LiOH solution of known concentration. The resulting gel was dried at 425 K overnight and heated to 865 K in air for two hours. The surface area of the resultant powder was 39 m^2/g. X-ray diffraction analysis* indicated β-$LiAlO_2$ to be the major phase, with only minor phases of unreacted γ-Al_2O_3 and Li_2CO_3. The SEMs showed that the powder consisted of about 50% small, sphere-like particles (<0.5 μm) and about 50% agglomerates (about 3-5 μm) composed of sphere-like particles. To date, samples taken after 48, 275, 665, and 1023 h at 950 K have shown no transformation to γ-$LiAlO_2$. The SEMs of the $LiAlO_2$ after 48, 275, and 665 h show the same general characteristics as those of the starting material.

During this past quarter, studies to determine the transformation temperature of the $LiAlO_2$ allotropes have been initiated. A Du Pont 990 thermal analyzer with a high-temperature differential-thermal-analyzer (DTA) cell (1475 K) was calibrated with a gold melting point standard (mp, 1336 K). In these first experiments, the sample cup contained about 30 mg of essentially pure β-$LiAlO_2$ and the reference cup contained about 30 mg γ-$LiAlO_2$; both cups were heated at 10 K/min in air to 1000 K. Figure 6 is the thermogram obtained under these conditions and shows only one event, an endotherm beginning at about 954 K. X-ray diffraction analysis confirmed that the β-$LiAlO_2$ in the sample cup had transformed to γ-$LiAlO_2$. The heating rate was increased to 20 K/min, in a separate experiment, but did not result in any discernible temperature shifts in the endotherm.

In related experiments, a Rigaku DSC (differential scanning calorimeter) was used to determine the transformation temperature from β- to γ-$LiAlO_2$; three separate determinations were made. Table 9 gives the results of these DSC determinations; the results of the DTA thermograms are also included in

*X-ray analyses performed by B. S. Tani, Analytical Chemistry Section, ANL.

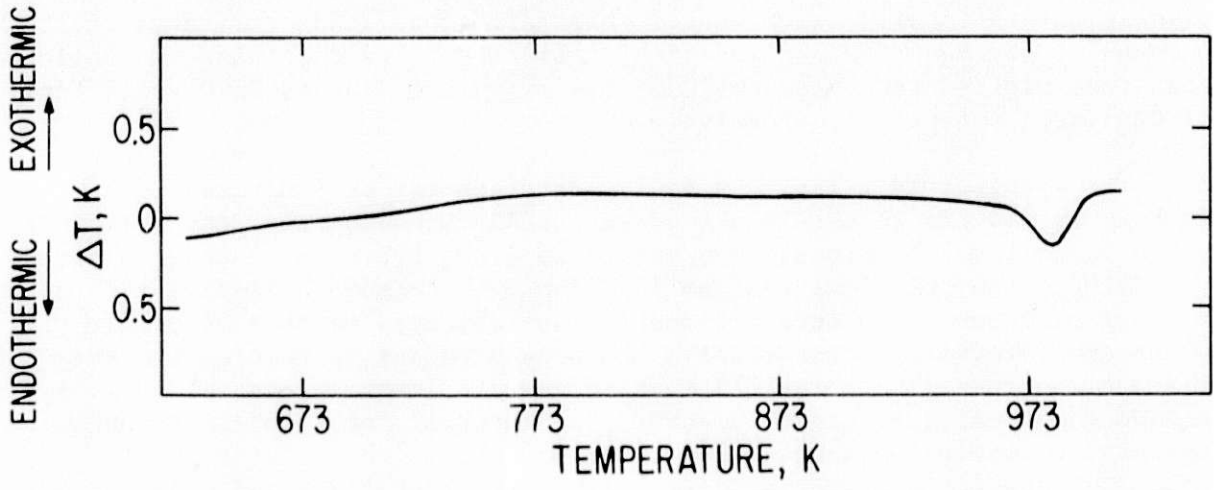

Fig. 6. Thermogram of Pure β-$LiAlO_2$ Transformation to γ-$LiAlO_2$

Table 9. Transformation Temperature of Pure β-$LiAlO_2$ to γ-$LiAlO_2$

Method	Weight of $LiAlO_2$, mg	Reference Material	Environment	Heating Rate	Transformation Temperature, K
DSC	25.1	γ-Al_2O_3	air	8 mcal/sec	960
DSC	29.2	γ-Al_2O_3	argon	4 mcal/sec	966
DSC	27.2	γ-Al_2O_3	air	2 mcal/sec	957
DTA	~30	γ-$LiAlO_2$	air	20 K/min	958
DTA	~30	γ-$LiAlO_2$	air	10 K/min	954
DTA	~30	γ-$LiAlO_2$	air	10 K/min	961

this table for comparison. There is generally good agreement among the results obtained with the DSC; furthermore, these results are in good agreement with those obtained from DTA. The average transformation temperature for essentially pure β-$LiAlO_2$ to γ-$LiAlO_2$ (both DSC and DTA) was 959 ± 4 K. Cooling curves obtained from both instruments show that the transformation was not reversible.

B. Thermomechanical Testing

The thermomechanical behavior of five small (about 13-mm dia) hot-pressed pellets containing $LiAlO_2$ and Li_2CO_3-K_2CO_3 eutectic was monitored in the dilatometer (ANL-79-84, p. 27). Three pellets containing γ-$LiAlO_2$ and 69.1 vol % (62.5 wt %) eutectic, which is the mixture currently used for the

tile in our test cells, were tested under different loads to assess their mechanical strength for use in a fuel cell tile. The remaining two pellets contained high-surface-area β-$LiAlO_2$ (39 m^2/g) and 7.6 and 22.0 vol % (solid) Li_2CO_3-K_2CO_3 eutectic, respectively.

The electrolyte tiles in a fuel cell stack may be subjected to stresses as high as 350 kPa to obtain a good wet seal. Consequently, the pellet of γ-$LiAlO_2$/69.1 vol % eutectic was heated to about 775 K while under a stress of 209 kPa, the practical maximum load for our thermomechanical apparatus. A slump/permanent structure deformation was measured to be >50% over a 30 second interval. Subsequently, the second pellet containing the same mixture was heated to about 775 K while under a lower stress, 41 kPa. Again a >50% compression occurred; however, the interval for complete compression extended to several minutes. The third pellet, which contained a new γ-$LiAlO_2$/eutectic mixture, also was tested at about 775 K and under 41 kPa stress with the same results, i.e., the compression occurring over several minutes. These results suggest that it would be desirable to apply the compressive load to the cell at the eutectic melting temperature (about 765 K), before the electrodes have extracted much electrolyte from the tile and the tile is still plastic.

The coefficient of linear thermal expansion determined for the temperature range from room temperature to 650 K on the two pellets containing high-surface-area β-$LiAlO_2$ and 7.6 and 22.0 vol % (solid) Li_2CO_3-K_2CO_3 eutectic was 11.4 ± 1.9 × 10^{-6}/°C and 16.3 ± 1.5 × 10^{-6}/°C, respectively. The measured total creep after 100 h at 925 K and 98.5 kPa stress was 0.14% for the pellet containing 7.6 vol % eutectic and 0.12% for the pellet containing 22 vol % eutectic. About 50-60% of the creep occurred in the first ten hours at temperature. This trend was observed and reported previously (ANL-79-110, p. 23) for pellets containing various mixtures of high- or low-surface-area γ-$LiAlO_2$ and electrolyte.

VI. CELL TESTING
(J. W. Sim and J. L. Smith)

Two laboratory-scale cells were tested using "boiler-plate" hardware and paste-type electrolyte structures (tiles), namely, SQ-14 and -15.

Cell SQ-14 was assembled with a Kanthal-screen reinforced tile, T-159-101 (γ-$LiAlO_2$/62.5 wt % Li_2CO_3-K_2CO_3), and with an anode that had been prewet with hydroxides. It was run for approximately 200 h and had the lowest measured cell resistance (11.5 mΩ) in the SQ series to that time. The performance was comparable to that of the best performing previous cell, SQ-9, in spite of severe wet-seal leakage. Posttest examination of cell SQ-14 revealed gaps of as much as 0.18 mm (0.007 in.) between the electrode housings and the tile. The anode current collector suffered corrosion damage at the edges near the outlet. The cathode housing and current collector had visible rust near the inlet. In this test, a holding stress of 35 kPa (5 psi) was applied at 21 h of operation. At this time, some of the electrolyte would have migrated from the tile, making the tile more resistant to plastic deformation than it had been earlier. An earlier application of the holding force might have caused the tile to flow, establishing a wet seal and also resulting in other cell performance improvements due to better conformance of the tile to dimensional irregularities.

The next test cell, SQ-15, was basically identical to that of SQ-14. The primary differences were that the tile, T-1-24 (γ-$LiAlO_2$/62.5 wt % Li_2CO_3-K_2CO_3), was not reinforced and that the cell housing ribs were scraped as well as sand-blasted in pre-assembly cleaning operations. The scraping tends to flatten, rather than enhance, irregularities and hence should result in better metal-to-metal contact between the housing and current collector (ANL-78-40, p. 25-29). The tile had approximately 0.15 mm (0.006 in.) taper in one diagonal direction and 0.04 mm (0.0015 in.) in the other. X-ray radiography indicated a uniform density.

At approximately 3 h of operation, when the tile had just exceeded the electrolyte melting point, an external holding force was applied. This procedure resulted in improved sealing at both the anode and cathode wet seals. This cell had the lowest measured resistance of the SQ series (8 mΩ). It also had the best performance. However, in past SQ cells, a gradual improvement in performance normally occurred over the first two hundred hours, whereas the performance of this cell stabilized in well under fifty hours. Disassembly of this cell revealed that the early application of an external holding force had caused plastic deformation of the tile and, hence, establishment of a wet seal. The anode current collector was rather severely corroded. This corrosion was the cause of anode wet-seal degradation observed at about two hundred hours. The corrosion was worst along the edges of the current collector, toward the outlet. Areas where obvious gaps were observed at the anode wet seal seemed to correspond with the areas of worst corrosion. The cathode wet seal had not deteriorated at the time of test termination. The tile had taken on a rusty hue, perhaps iron oxide from the cathode current collector and housing.

It currently appears that several steps should be taken to improve cell performance further. The early application of an external holding force appears to result in a good wet seal and will be done on future tests. Among other things, low cell resistance depends on good metal-to-metal contact between the cell housing and current collector; this depends on both the housing and current collector being flat and free of oxides. In addition to occasional remachining of the cell housings, it may be desirable to run reducing gases through the cell until after the holding force has been applied. The corrosion problem with the anode current collector can be eliminated with nickel parts or nickel-plated stainless steel parts. The effect of operational changes on the 316 stainless steel parts will also be investigated.

APPENDIX

INTRODUCTION TO ACOUSTIC MICROSCOPY

by

D. S. Kupperman,* D. E. Yuhas,† C. Vorres,† and R. B. Poeppel*

An acoustic microscope visually reveals localized changes in elastic properties of materials by measuring the point-by-point interactions of the specimen to a periodic stress wave (acoustic wave). Thus, the physical properties of matter which govern sound propagation (namely, compressibility, density, and viscoelasticity) are translated into acoustic micrographs. The sonically transparent nature of most materials permits interior examination in optically opaque samples. Subsurface defects, flaws, inclusions, and unbonded areas are particularly amenable to detection by acoustic microscopy.

The notion of acoustic microscopy dates back to 1936 when S. Y. Sokolov[1] proposed a device for producing magnified views of structures with 3 GHz soundwaves. However, due to severe technological limitations, no such instrument could be constructed at the time, and it was not until 1959 that Dunn and Fry[2] performed the first acoustic microscopy experiments, though not at very high frequencies. The scientific literature shows very little progress in acoustic microscopy following the Fry and Dunn experiments up until about the early 1970's, when two groups of investigators of acoustic microscopy emerged--one at Stanford University and the other at Zenith Radio Corporation. In 1973, the Stanford group began the development of a confocal pair of acoustic lenses to focus and detect ultrasonic energy.[3] Advancements to date have to do with achieving very high resolution, novel modes of imaging, and applications. This instrument is called a Scanning Acoustic Microscope (SAM). In 1970, the Zenith group began to pursue a scanning laser detection system for microscopy. In early 1974, the Zenith activity was shifted to a new organization, Sonoscan, Inc., where practical aspects of the instrument were developed. This instrument is called the scanning laser acoustic microscope (SLAM). A review of work to date in acoustic microscopy research has been presented by Kessler and Yuhas.[4]

In the Sonomicroscope‡ SLAM, a specimen is viewed by placing it on a stage where it is insonified with plane acoustic waves (instead of focused waves as in SAM) and illuminated with laser light.[5,6] A block diagram of this system[7] is shown in Fig. 1. Within the sample, the sound is scattered and absorbed according to the internal elastic microstructure. The principle upon which the laser beam is employed as a detector is based upon the minute displacements which occur as the soundwave propagates. As shown in Fig. 2, an optically reflective surface placed in the sound field will become distorted in proportion to the localized sound pressure. The distortions are dynamic in that the pressure wave is periodic and the mirror displacements accurately follow the wave amplitude and phase. At every instant of time, the mirror surface is an optical phase replica of the sound field. The laser is used to measure the degree of regional distortion. By electronically

---

*Materials Science Division, ANL.

†Sonoscan, Inc., Bensenville, IL 60106.

‡Trade name - Sonoscan, Inc.

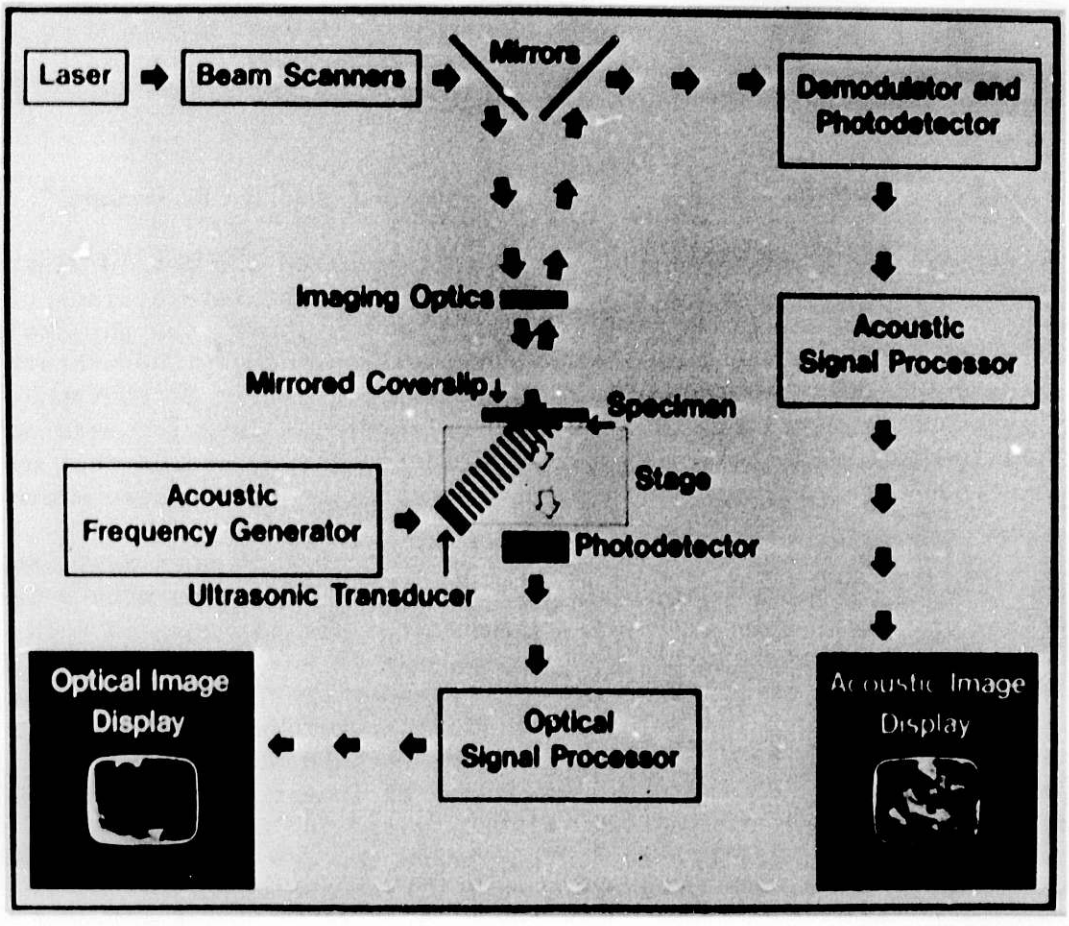

Fig. 1. Block Diagram of Acoustic Microscope.
ANL Neg. No. 308-80-102

magnifying the area of laser scan to the size of a CRT (cathode ray tube) monitor and by modulating the brightness of the display, the acoustic micrograph is made visible. If the sample is made of a solid substance that can be optically polished (as for metallurgical examination), the sample is viewed directly with the laser. However, the electrolyte tiles are not polished and, therefore, a plastic mirror (coverslip) is placed in contact with the sample to relay the sonic information into the laser beam.

The laser detection process can be explained further with reference to Fig. 2. A light beam striking the mirror will be reflected at an angle equal to the incident angle. When the surface is tilted by an amount proportional to the sound pressure, the reflected light is angularly modulated (spatial). If all the reflected light is captured by a photodiode, its electrical output signal will be a dc level only because the light power reaching the detector will not change as a function of angle. However, if part of the light beam is blocked by an obstacle (or knife-edge), then the amount of light reaching the photodiode will depend upon the instantaneous angular position of the beam. Thus, the electrical signal output will now consist of a dc component plus a small ac component that is coherent with the acoustic amplitude.

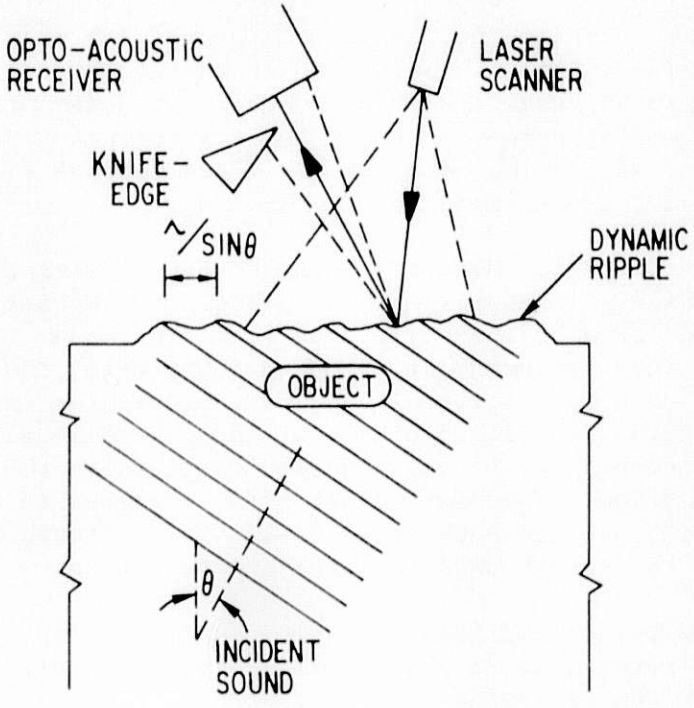

Fig. 2. Schematic Representation of Acoustic Microscope, Acoustic Cell, and Scanner Laser Beam

As a by-product of the laser scanning technique, an optical image of the sample is obtained simulataneously, as indicated in Fig. 1. In the case of optically translucent samples, such as biological material and some solid materials, a "partially silvered" coverslip is employed so that a fraction of the probing laser light can penetrate the mirror and sample. This transmitted light is detected and the resulting signal fed to an adjacent CRT monitor, thus constituting an optical image. In the case of a reflective polished specimen, such as a metal prepared for metallographic examination, an optical reflection image is produced. The importance of the simultaneous optical image is very great to the user, for it permits newly obtained acoustical information to be compared immediately to a familiar optical reference. This is accomplished without repositioning the sample or disturbing its environmental conditions.

The acoustic images are produced at a rate of 30 per second; therefore, dynamic effects such as crack propagation in mechanical stressed materials can be recorded.

Three modes of operation are available:

(1) Normal Mode. Acoustic through transmission microscopy at single acoustic frequency. Data output is in the form of acoustic transmission variations, with bright regions of the micrograph corresponding to good acoustic transmission and dark regions corresponding to poor acoustic transmission.

(2) Frequency Modulated. Swept insonification imaging with variable deviation control. Data output is in the form of acoustic transmission variation. The intensity variations of the acoustic transmission are interpreted in the same manner as normal mode. As a result of swept frequency insonification, coherent speckle (structures which result from coherent energy impinging on a diffuse substance) effects, evident in normal mode, are eliminated.

(3) Interferometric Mode. Acoustic through transmission plus acoustic phase detection. In addition to displaying the acoustic intensity distribution throughout the field of view, the sonomicroscope provides an acoustic interference mode of operation. Here, the acoustic phase is measured on a T.V. screen as the wave propagates through various structures within the field of view. Thus, very localized velocity of sound measurements can be made and fluctuations in the "elastic index" can be documented. The elastic index is analogous to the optical index of refraction, but has much more significance because of its great sensitivity to density and/or elasticity variations.

The shift to any of the SLAM operating modes is electronically controlled; and, therefore, no sample repositioning is necessary. Data analysis is illustrated in the following examples.

A normal-mode acoustic micrograph taken on a 7-mm-thick (acoustic energy propagated through 7 mm of material) hot-pressed silicon nitride disc is shown in Fig. 3. The sample has less than 1% porosity. In normal mode imaging, intensity variaitons correspond to acoustic transmission variations--with bright regions corresponding to good acoustic transmission (low attenuation) and dark regions corresponding to poor acoustic transmission (high attenuation). The intensity is relatively uniform in this microgrph, indicative of uniform acoustic transmission. The vertical striations observed are a result of the rough surface texture of the sample.

A normal-mode acoustic micrograph taken on a 7-mm-thick hot-pressed silicon nitride disc with approximately 8% porosity is shown in Fig. 4. The dark, highly attenuated region results from acoustic energy being scattered and reflected off embedded clusters of pores. Evidence of surface texture is manifested by the diagonal striations.

A normal mode of acoustic micrograph taken on a reaction-sintered silicon nitride turbine blade is shown in Fig. 5. The disrupted transmission, indicated by intensity variations, results from the porosity of the silicon nitride. It is instructive to compare the structure of the hot-pressed sample (Fig. 3) to that of the sintered one.

An acoustic interferogram taken on a 7-mm-thick hot-pressed silicon nitride sample with less than 1% porosity is shown in Fig. 6. The black vertical lines are interferogram fringes. The spacing between fringes is 85 microns. In a uniform sonic velocity field, the fringes are straight, continuous, and parallel. At a localized region of lower sonic velocity, the fringes shift to the left; high sonic velocity regions are characterized by a fringe shift to the right. This uniform (very low porosity) silicon nitride sample is characterized by uniform sonic velocity. The intensity variations seen beneath the fringes are interpreted in the same manner as in the normal mode.

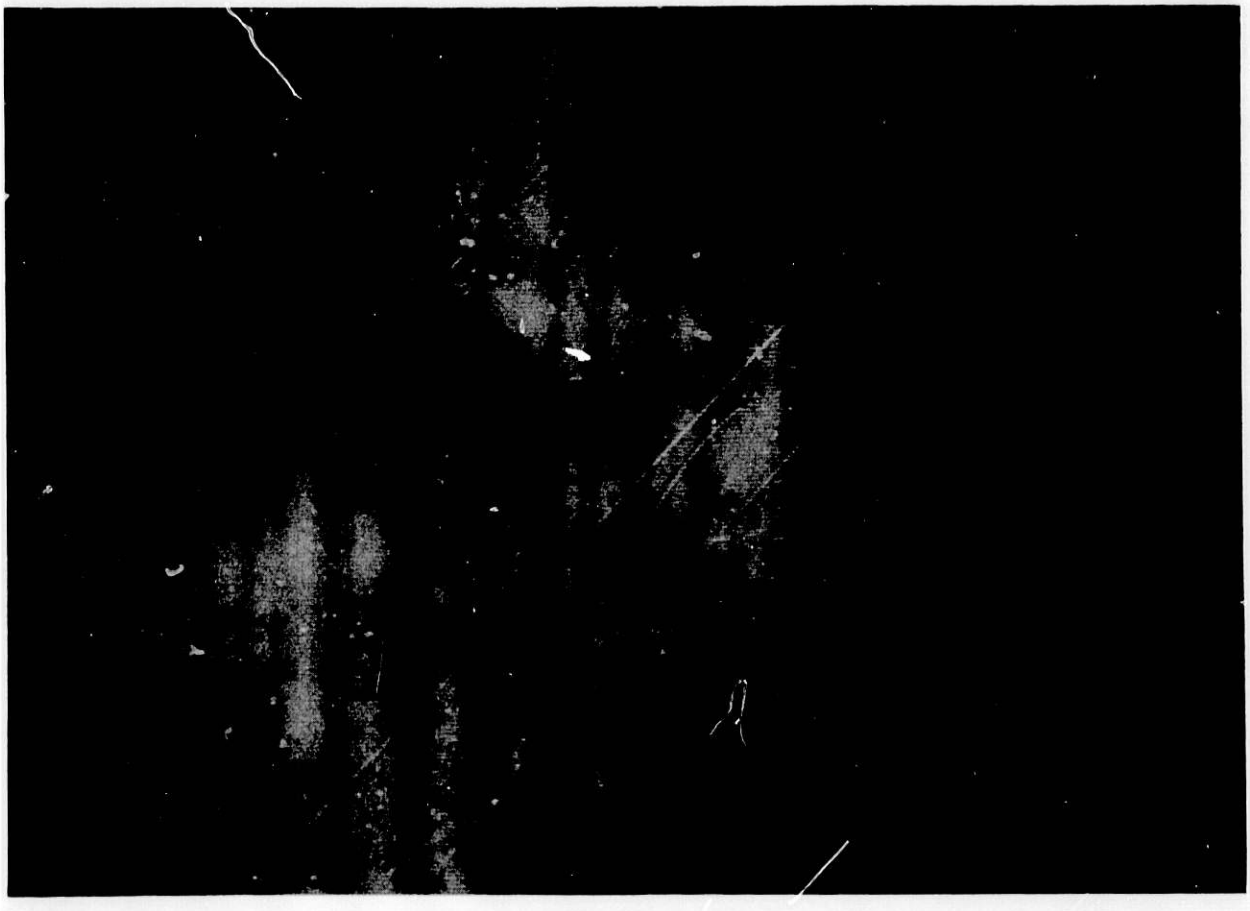

Fig. 3. Acoustic Micrograph of Hot-pressed Silicon Nitride. (The horizontal field of view is 2.5 mm.)

Fig. 4. Acoustic Micrograph of Hot-Pressed Silicon Nitride Showing Porosity Region. (The horizontal field of view is 3 mm.)

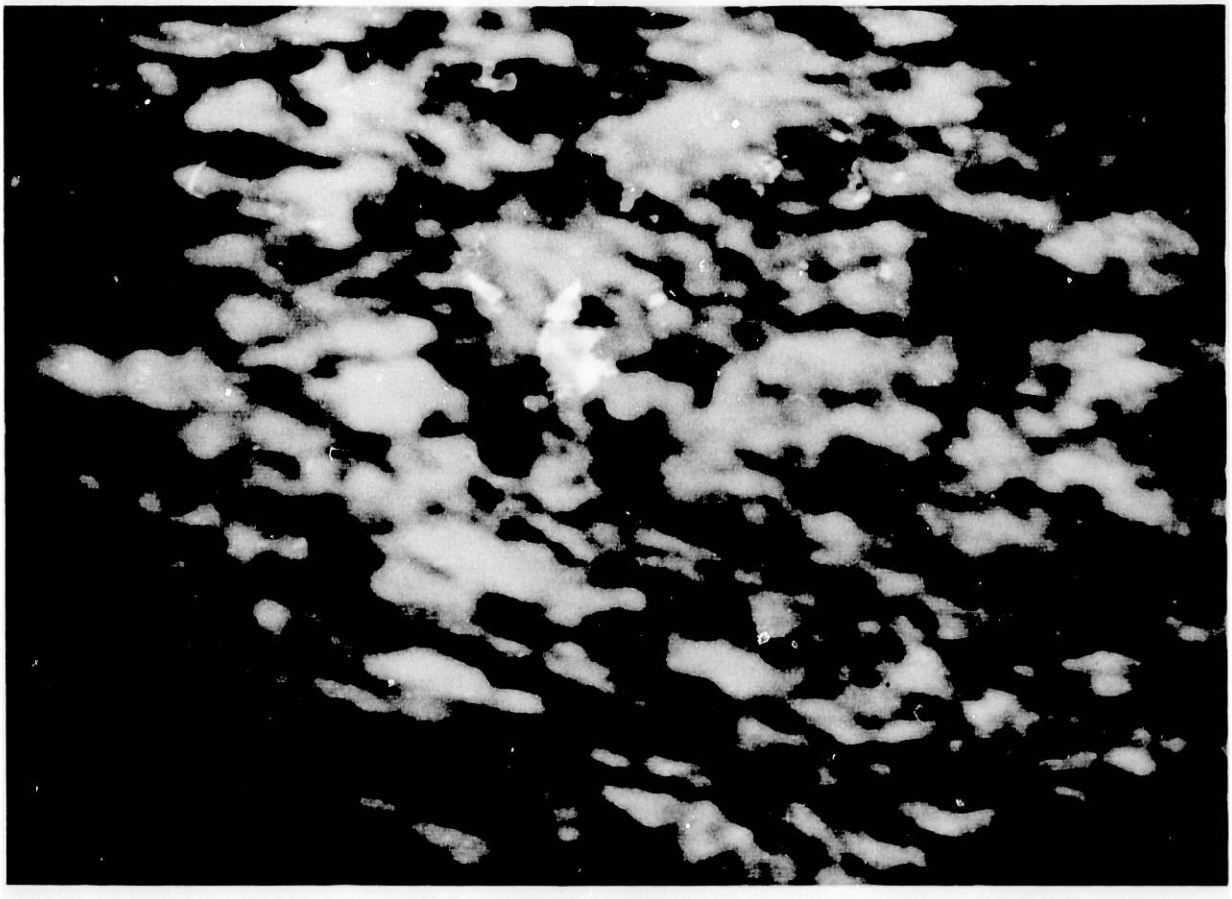

Fig. 5. Acoustic Micrograph of Reaction-Sintered Silicon Nitride. (The horizontal field of view is 3 mm.)

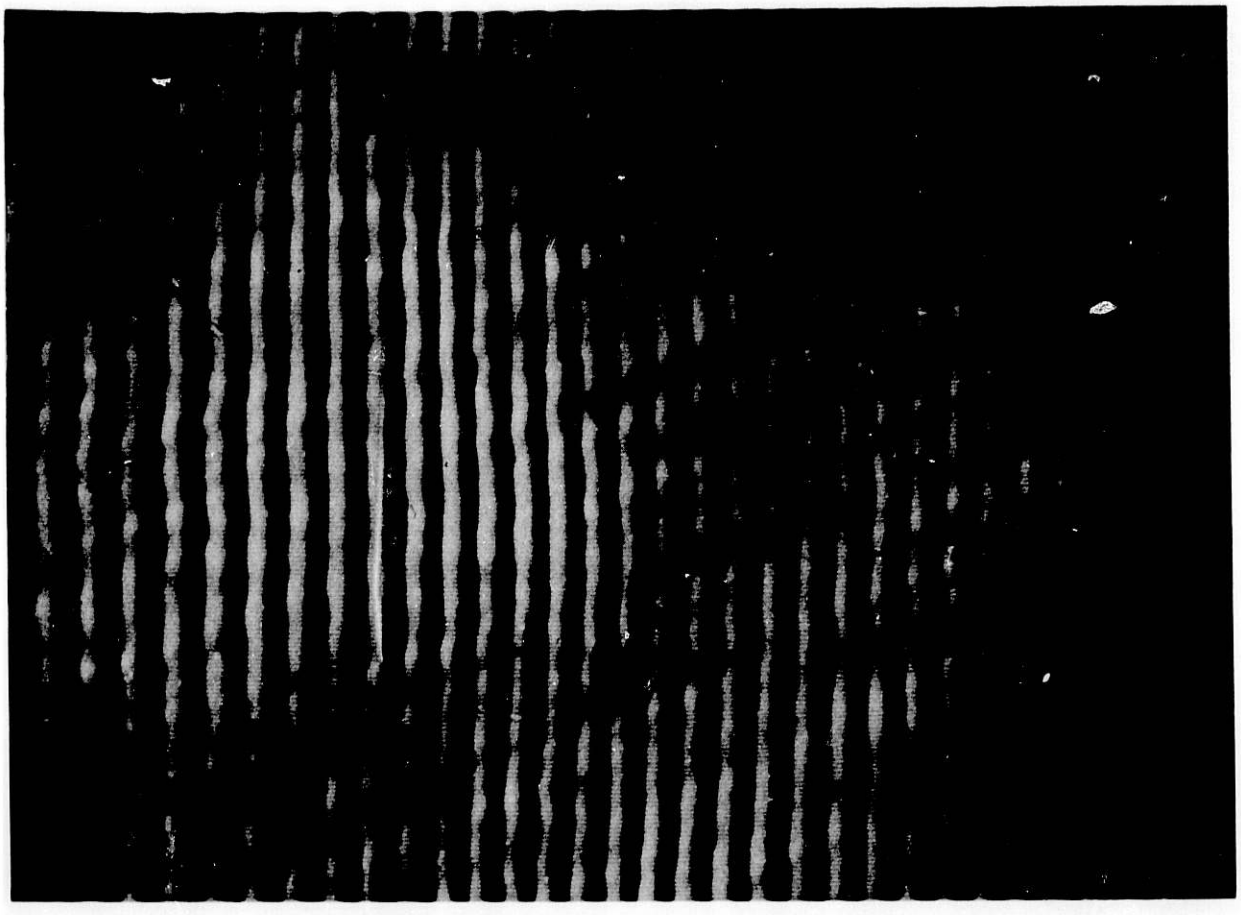

Fig. 6. Acoustic Interferogram of Hot-Pressed Silicon Nitride. (The horizontal field of view is 2.5 mm.)

Nonuniformities in sonic velocity lead to interferogram fringe shifts, which are shown in Fig. 7. By measuring the amount of fringe displacement, the magnitude of sonic velocity difference can be determined.

Figure 8 shows a normal micrograph and an interferogram of a crack in an alumina sample. The most dominant feature occurring in the vicinity of fractures is the attenuated shadow zone. A fracture interface leads to substantial sound scattering, thus producing a dark shadow to the right of the crack. Estimation of the crack extension is obtained by measuring the width of the shadow zone. Surface opening cracks have been detected acoustically, even though no evidence of fractures can be seen optically at high magnification.

Figure 9 shows a normal mode image of a 600-μm dia carbon inclusion embedded 5 mm below the surface of a 7-mm-thick hot-pressed silicon nitride sample. Solid inclusions are characterized by a dark diffraction ring surrounding a bright core zone.

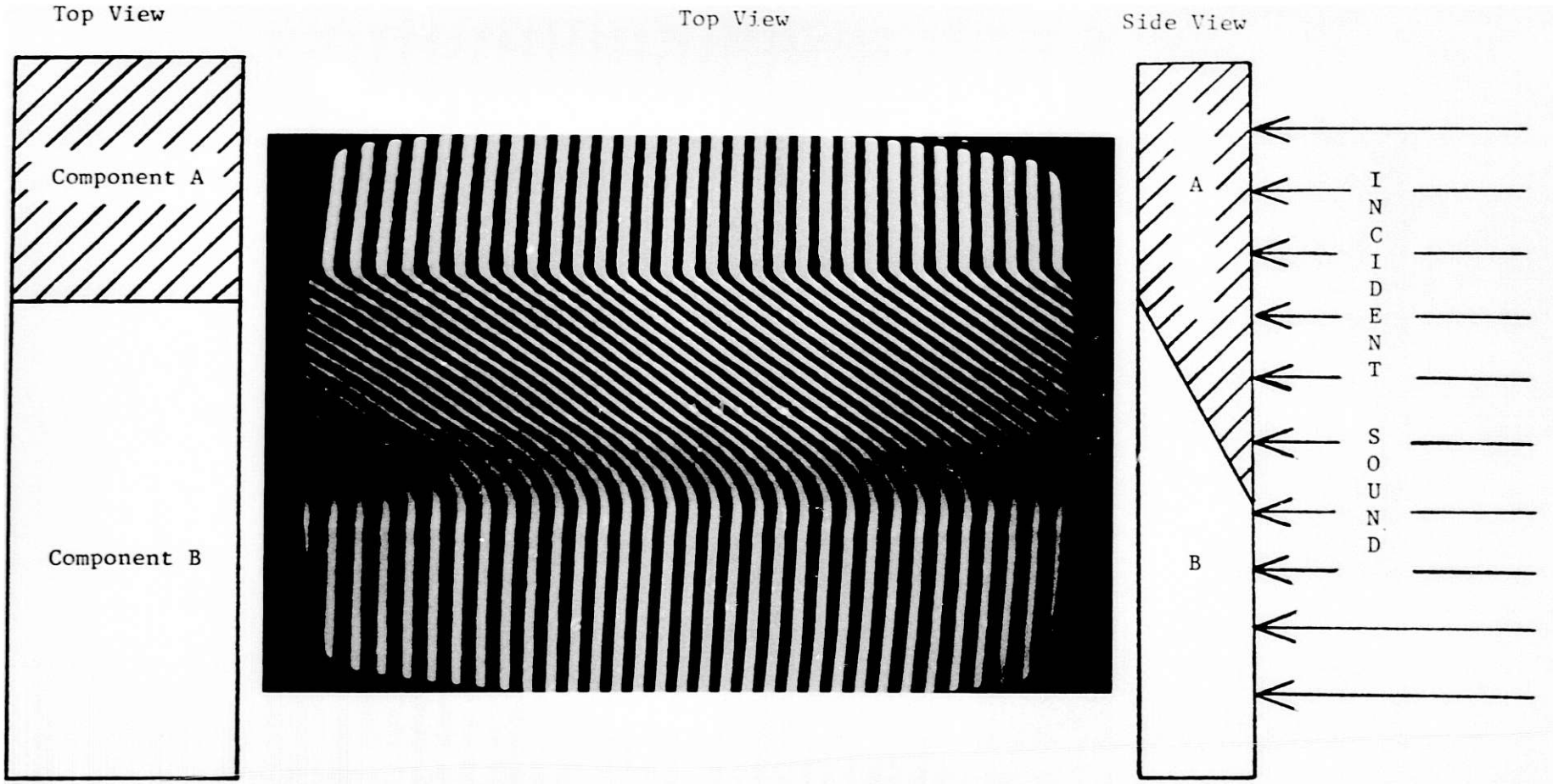

Fig. 7. Acoustic Interferogram of Wedge-jointed Dissimilar Materials

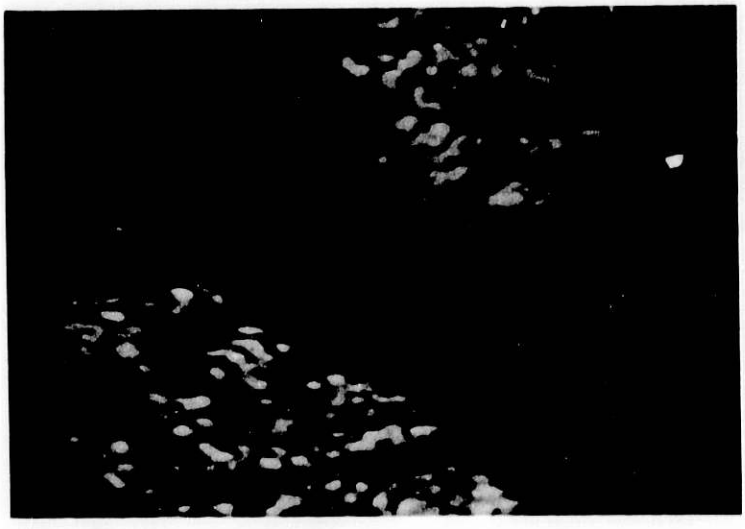

(a)

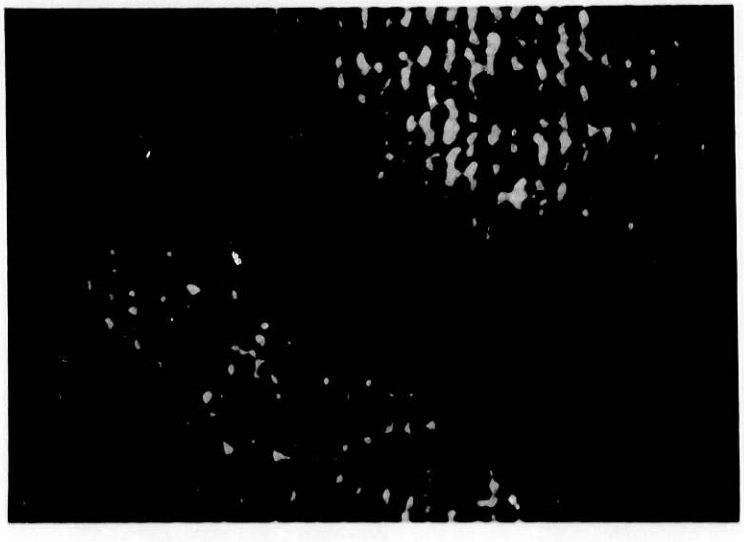

(b)

Fig. 8. Crack Detection in Alumina Sample.
(a) Normal Micrograph.
(b) Interferogram.

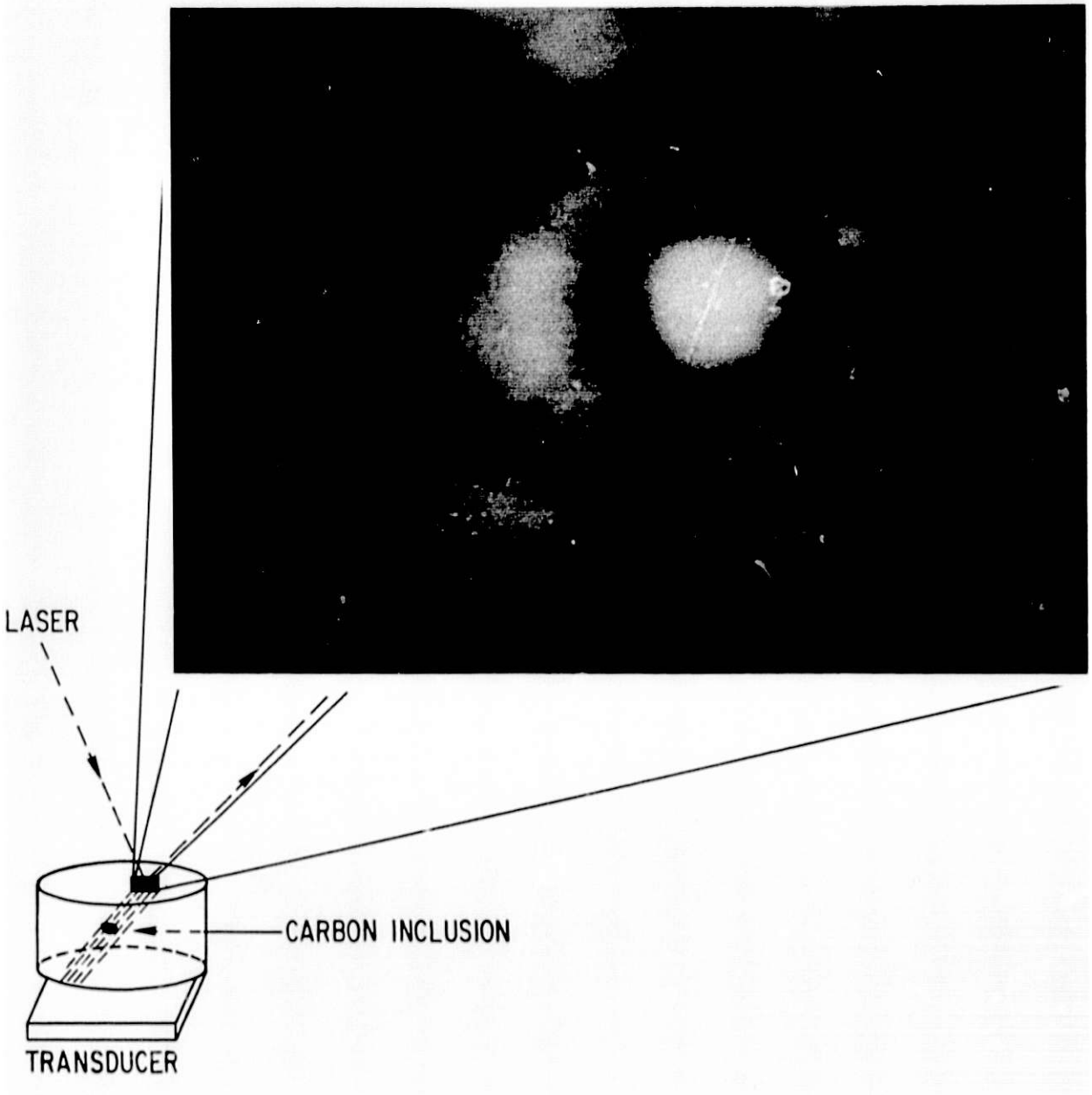

Fig. 9. Solid Inclusion (600 μm diameter) in Silicon Nitride

REFERENCES

1. S. Sokolov, USSR Patent No. 49 (Aug. 31, 1936); British Patent No. 477 139 (1937); and U.S. Patent No. 21 64 125 (1939).

2. F. Dunn, and W. J. Fry, Ultrasonic Absorption Microscope, J. Acoust. Soc. Amer., Vol. 31, No. 5, pp. 632-633 (May 1959).

3. J. Havlice, C. F. Quate, and B. Richardson, Visualization of Sound Beams in Quartz and Sapphire near 1 GHz, Paper 1-4 presented to the 1967 IEEE Ultrason. Symp., IEEE Trans. Sonics Ultrason., Vol. SU-15, p. 68 (1968).

4. L. Kessler, and D. Yuhas, Acoustic Microscopy-1979, Proc. of IEEE, Vol. 67, No. 4, pp. 526-536 (April 1979).

5. A. Korpel, L. W. Kessler, and P. R. Palermo, Acoustic Microscope Operating at 100 MHz, Nature, Vol. 232, No. 5306, pp. 110-111 (1971).

6. L. W. Kessler, A. Korpel, and P. R. Palermo, Simultaneous Acoustic and Optical Microscopy of Biological Specimens, Nature, Vol. 239, No. 5367, pp. 111-112 (1972).

7. L. W. Kessler, and D. E. Yuhas, Structural Perspective, Indust. Rev., Vol. 20, No. 1, 53-56 (1978).

8. S. A. Goss, and W. D. O'Brien, Direct Ultrasonic Velocity Measurements of Mammalian Collagen Threads, J. Acoust. Soc. Am., 65, 507-511 (1977).